The Astrophysical Journal, 960:80 (16pp), 2024 January 1 https://doi.org/10.3847/1538-4357/ad0cf3

Can Proton Beam Heating Flare Models Explain Sunquakes?

Viacheslav M. Sadykov[1], John T. Stefan[2], Alexander G. Kosovichev[2,3], Andrey M. Stejko[2], Adam F. Kowalski[4,5,6], Joel C. Allred[7], and Graham S. Kerr[7,8]
[1] Physics & Astronomy Department, Georgia State University, Atlanta, GA 30303, USA
[2] Center for Computational Heliophysics, Physics Department, New Jersey Institute of Technology, Newark, NJ 07102, USA
[3] NASA Ames Research Center, Moffett Field, CA 94035, USA
[4] National Solar Observatory, University of Colorado Boulder, 3665 Discovery Drive, Boulder, CO 80303, USA
[5] Department of Astrophysical and Planetary Sciences, University of Colorado, Boulder, 2000 Colorado Avenue, CO 80305, USA
[6] Laboratory for Atmospheric and Space Physics, University of Colorado Boulder, 3665 Discovery Drive, Boulder, CO 80303, USA
[7] NASA Goddard Space Flight Center, Solar Physics Laboratory, Code 671, Greenbelt, MD 20771, USA
[8] Department of Physics, Catholic University of America, 620 Michigan Avenue, Northeast, Washington, DC 20064, USA

Received 2023 June 22; revised 2023 November 14; accepted 2023 November 14; published 2023 December 28

Abstract

Solar Dynamics Observatory (SDO)/Helioseismic and Magnetic Imager (HMI) observations reveal a class of solar flares with substantial energy and momentum impacts in the photosphere, concurrent with white-light emission and helioseismic responses, known as sunquakes. Previous radiative hydrodynamic modeling has demonstrated the challenges of explaining sunquakes in the framework of the standard flare model of "electron beam" heating. One of the possibilities to explain the sunquakes and other signatures of the photospheric impact is to consider additional heating mechanisms involved in solar flares, for example via flare-accelerated protons. In this work, we analyze a set of single-loop Fokker–Planck and radiative hydrodynamics RADYN+FP simulations where the atmosphere is heated by nonthermal power-law-distributed proton beams which can penetrate deeper than the electron beams into the low atmospheric layers. Using the output of the RADYN models, we calculate synthetic Fe I 6173 Å line Stokes profiles and from those the line-of-sight observables of the SDO/HMI instrument, as well as the 3D helioseismic response, and compare them with the corresponding observational characteristics. These initial results show that the models with proton beam heating can produce the enhancement of the HMI continuum observable and explain qualitatively the generation of sunquakes. The continuum observable enhancement is evident in all models but is more prominent in ones with $E_c \geqslant 500$ keV. In contrast, the models with $E_c \leqslant 100$ keV provide a stronger sunquake-like helioseismic impact according to the 3D acoustic modeling, suggesting that low-energy (deka- and hecto-keV) protons have an important role in the generation of sunquakes.

Unified Astronomy Thesaurus concepts: Solar white-light flares (1983); Helioseismology (709); Hydrodynamical simulations (767); Spectropolarimetry (1973)

1. Introduction

The energy release process in solar flares affects all layers of the solar atmosphere, from the photosphere to the corona. The standard "thick-target" flare model assumes that a substantial part of the flare energy is released in the solar corona in the form of a high-energy (deka-keV) electron distribution traveling downward along magnetic field lines and heating the upper chromosphere (Hudson 1972). Radiative hydrodynamic modeling of the atmospheric response to the electron beam heating, initiated by Kostiuk & Pikelner (1975), revealed upflows of chromospheric plasma into the flare loops (commonly referred to as "chromospheric evaporation"), accompanied by a dense downward-propagating shock (chromospheric "condensation"; Livshits et al. 1981; Fisher et al. 1985; Kosovichev 1986). These hydrodynamic models found that the downward-moving shock quickly decays, within 60 s or so, which is borne out by observations (see also Ashfield & Longcope 2021; Ashfield et al. 2022; Kerr 2022, 2023). This has the implication that the downward-moving shock is insufficient for explaining deep perturbations of the solar photosphere. Livshits et al. (1981) suggested that the white-light emission can be produced by chromospheric condensations (see also Kowalski et al. 2015, 2017, who studied both solar and stellar models of continuum emission from chromospheric condensations). The radiative back-warming process can also play an important role in white-light emission generation (Machado et al. 1989).

Using observations from the Michelson Doppler Imager on the Solar and Heliospheric Observatory (Scherrer et al. 1995), Kosovichev & Zharkova (1998) showed that flares can produce a significant impact in the photosphere, which is sufficient for the generation of helioseismic waves ("sunquakes"). The localized impulsive impacts and sunquakes are also observed in the photospheric observations of the Helioseismic and Magnetic Imager (HMI) on board the Solar Dynamics Observatory (SDO; Scherrer et al. 2012). Such impacts are typically accompanied by enhancements of the continuum emission (for example, all 18 sunquake events studied by Buitrago-Casas et al. 2015 were accompanied by such enhancements), as well as strong variations in Doppler shift and magnetic field, and are identified as sunquake sources (Sharykin & Kosovichev 2020). In a recent work, Wu et al. (2023) suggested that the high-energy tail ($E_e > 300$ keV) of a nonthermal electron distribution is a preferred driver of the sunquakes. This result was obtained based on the analysis of 20 strong flares of Solar Cycle 24 and fitting the hard X-ray emission spectra observed by the Reuven Ramaty High-Energy Solar Spectroscopic Imager (RHESSI; Lin et al. 2002).

Recently, the flare community has made extensive use of radiative hydrodynamics simulations performed using the RADYN code, developed by Carlsson & Stein (1992) and adopted for flare modeling by Abbett & Hawley (1999) and Allred et al. (2005, 2015). In agreement with the earlier models, these RADYN simulations demonstrated that electron beams can only weakly affect the photospheric layers through direct heating. Sadykov et al. (2020) performed modeling of the Fe I 6173 Å Stokes profiles and corresponding SDO/HMI line-of-sight (LOS) observables for single-loop RADYN electron-beam-driven simulations. Those simulations were available as a part of the F-CHROMA[9] project (Carlsson et al. 2023). The highest HMI continuum intensity observable[10] enhancement of about 3%, accompanied by HMI observable Doppler velocities of ∼0.4 km s^{-1}, were found for the model with the total energy of $E_{\text{total}} = 10^{12}$ erg cm^{-2}, low cutoff energy of $E_c = 25$ keV, and a power-law spectral index $\delta = 3$. The electrons were injected for 20 s into the solar atmosphere in a triangular profile that peaked at $t = 10$ s for F-CHROMA models, so that, correspondingly, the average injected flux in that model was equal to $F_d = 5 \times 10^{10}$ erg cm^{-2} s^{-1}. While the perturbations of the SDO/HMI observables in that grid of simulations could not explain the SDO/HMI derived continuum intensity enhancements observed during white-light flares (10%–100% depending on the flare's soft X-ray class; Song & Tian 2018), models with higher electron beam fluxes (Kowalski 2022) are expected to show a significant white-light emission. The F-CHROMA models also clearly do not result in the velocity signals of several kilometers per second which are needed for the initiation of sunquakes (Stefan & Kosovichev 2020).

One of the possibilities to explain the deep perturbations of the photosphere, including sunquakes, is to consider additional heating mechanisms involved in solar flares, e.g., Alfvén wave heating (Kerr et al. 2016; Reep & Russell 2016) and heating by nonthermal proton beams (Procházka et al. 2018). It is likely that nonthermal protons are present in flares, and may even carry energy equivalent to that of the nonthermal electron distribution (Emslie et al. 2012). However, largely owing to poor constraints on the properties of the distribution, they are often ignored in flare modelings, and numerical studies of their role in the Sun's atmospheric response to flares are rare. For further discussion, see the introduction to Kerr et al. (2023).

In this work, we analyze single-loop RADYN proton beam simulations in a wide set of beam parameters and impose the pressure perturbations from these models into the 3D helioseismic model of sunquakes (Stefan & Kosovichev 2020). Our goal is to answer the question: Can single-loop RADYN proton heating simulations, coupled with the 3D acoustic model of the Sun, cause a photospheric impact and explain the initiation and propagation of helioseismic signals detected in sunquakes? The paper is structured as follows. Section 2 describes RADYN proton-beam-heating simulations, synthesis of the Fe I 6173 Å line profiles and SDO/HMI LOS observables for these simulations, and the related results. Section 3 describes the development of the acoustic model simulations driven by the perturbations imposed from the RADYN models and the related results. A summary of the paper's results followed by discussion is presented in Section 4.

2. Modeling Fe I 6173 Å Stokes Profiles and SDO/HMI Observables from RADYN Proton Beam Simulations

2.1. Description of RADYN Proton Beam Heating Runs

We employ the unified computational model for solar and stellar flares, RADYN (Allred et al. 2015), which self-consistently combines the equations of radiation transport, nonequilibrium atomic level populations, charge conservation, and hydrodynamics following the injection of flare energy into one leg of a semicircular loop, assumed to be symmetrical. RADYN was recently coupled with the FP code (Allred et al. 2020), which models the transport of high-energy particles from their injection in the solar corona to thermalization in the low atmosphere by solving the Fokker–Planck equation. The FP code models the evolution of the distribution function taking into account Coulomb collisions, nonuniform ionization, magnetic mirroring, the return electric currents, and synchrotron emission reactions, and offers an improvement upon prior implementations of nonthermal particles in RADYN. FP implements Coulomb collisions of nonthermal particles with an ambient plasma of arbitrary temperature and is applicable throughout the cold-target to warm-target regimes. Importantly for this study, for nonthermal protons with energies in the deka- to hecto-keV range, the ambient plasma is typically a warm target, which is much less effective at slowing the protons than cold-target collisions (Tamres et al. 1986).

In this work, we take advantage of the proton-beam-heating simulation grid computed for the series of studies recently started by Kerr et al. (2023). All RADYN proton beam runs analyzed in this work have approximately the same energy flux rates, $F_d = 10^{11}$ erg cm^{-2} s^{-1}, with two values for the energy power-law spectral indexes, $\delta = 3$ and 5, and eight values for the low-energy cutoff, $E_c = 25$, 50, 100, 150, 250, 500, 1000, and 3000 keV. The proton beam was injected into the atmosphere during the first 20 s of each simulation, after which the atmosphere evolved for an additional 80 s. Of these 16 total runs, 15 are considered here. The run, parameterized by $F_d = 10^{11}$ erg cm^{-2} s^{-1}, $\delta = 5$, and $E_c = 25$ keV, required a very small time step due to large perturbations of the atmosphere driven by beam heating, and was performed for a shorter duration. The overall properties of the completed runs are summarized in Tables 1 and 2. Note that the pre-flare atmosphere used in the F-CHROMA grid of simulations is rather different than that used here. The pre-flare atmosphere used in the F-CHROMA database is a VALC-like atmosphere, with a 1 MK corona and chromospheric temperature plateau. The chromospheric structure is maintained by nonradiative heating added to the simulation when beam heating is not present, and its construction is described in Carlsson et al. (2023). The pre-flare atmosphere used in Kerr et al. (2023) and our study of proton beam heating is an atmosphere in radiative equilibrium such that additional heating is only added to maintain the corona and photosphere. It has an apex temperature of 3 MK and is denser than the VALC-like atmosphere, with a transition region located at a deeper geometric altitude. Allred et al. (2015) describes the construction of this atmosphere. The difference between the vertical profiles of the initial atmospheres is illustrated in Figure 1. In addition, the energy flux is injected at a faster rate than for the

---

[9] https://star.pst.qub.ac.uk/wiki/public/solarmodels/start.html

[10] Hereafter, when we refer to HMI's continuum intensity observable we drop the "HMI."

Table 1

Properties of the Atmosphere and the Fe I 6173 Å Line Formation for RADYN Proton Beam Simulations with $\delta = 3$, $F_d = 10^{11}$ erg cm^{-2} s^{-1}

Model	Model Properties and Height	$\frac{\max(T)}{T_0}$	$\frac{\max(p)}{p_0}$	$\max(v_z)$ (km s^{-1})	$\min(v_z)$ (km s^{-1})	$\frac{\max(I_c)}{I_{c0}}$	$\frac{\max(I_d)}{I_{c0}}$	$\max(v_D)$ (km s^{-1})	$\min(v_D)$ (km s^{-1})	$\max(\tau_{I_c}{=}1)$ (km)	$\max(\tau_{I_d}{=}1)$ (km)
1	$E_c = 25$ keV, $\delta = 3$, $h = 100$ km	1.043	1.089	0.000	−0.517	1.077	0.497	0.022	−0.307	15	265
	$\cdots$, $h = 300$ km	1.125	1.267	0.338	−1.725	…	…	…	…	…	…
2	$E_c = 50$ keV, $\delta = 3$, $h = 100$ km	1.041	1.068	0.025	−0.368	1.073	0.513	0.034	−0.243	15	265
	$\cdots$, $h = 300$ km	1.109	1.244	0.523	−1.349	…	…	…	…	…	…
3	$E_c = 100$ keV, $\delta = 3$, $h = 100$ km	1.041	1.041	0.011	−0.162	1.070	0.517	0.168	−0.132	15	265
	$\cdots$, $h = 300$ km	1.068	1.163	0.271	−0.717	…	…	…	…	…	…
4	$E_c = 150$ keV, $\delta = 3$,$h = 100$ km	1.052	1.037	0.028	−0.099	1.082	0.488	0.150	−0.081	16	265
	$\cdots$, $h = 300$ km	1.072	1.109	0.225	−0.453	…	…	…	…	…	…
5	$E_c = 250$ keV, $\delta = 3$, $h = 100$ km	1.057	1.038	0.033	−0.021	1.090	0.456	0.117	−0.032	17	265
	$\cdots$, $h = 300$ km	1.086	1.109	0.244	−0.289	…	…	…	…	…	…
6	$E_c = 500$ keV, $\delta = 3$, $h = 100$ km	1.077	1.063	0.026	−0.271	1.155	0.376	0.025	−0.129	22	271
	$\cdots$, $h = 300$ km	1.156	1.328	0.316	−0.363	…	…	…	…	…	…
7	$E_c = 1000$ keV, $\delta = 3$, $h = 100$ km	1.087	1.067	0.045	0.000	1.174	0.303	0.082	−0.091	26	271
	$\cdots$, $h = 300$ km	1.195	1.211	0.541	−0.317	…	…	…	…	…	…
8	$E_c = 3000$ keV, $\delta = 3$, $h = 100$ km	1.166	1.143	0.121	−0.011	1.421	0.141	0.167	−0.686	53	343
	$\cdots$, $h = 300$ km	1.316	1.354	0.975	−0.509	…	…	…	…	…	…

Note. The subscript "0" denotes the parameter value at $t = 0$ s. The "min" and "max" operators return the minimum and the maximum values of the parameters during the run. I_c denotes the continuum near the line, I_d the line depth (measured as the difference between the line continuum and the smallest intensity across the line), τ_{I_c} the optical depth for the continuum near the Fe I 6173 Å line, and τ_{I_d} the optical depth for the line core.

Table 2

Same as Table 1 but for the Models with $\delta = 5$, $F_d = 10^{11}$ erg cm^{-2} s^{-1}

Model	Model Properties and Height	$\frac{\max(T)}{T_0}$	$\frac{\max(p)}{p_0}$	$\max(v_z)$ (km s^{-1})	$\min(v_z)$ (km s^{-1})	$\frac{\max(I_c)}{I_{c0}}$	$\frac{\max(I_d)}{I_{c0}}$	$\max(v_D)$ (km s^{-1})	$\min(v_D)$ (km s^{-1})	$\max(\tau_{I_c} = 1)$ (km)	$\max(\tau_{I_d} = 1)$ (km)
9	$E_c = 50$ keV, $\delta = 5$, $h = 100$ km	1.065	1.161	0.000	−0.794	1.122	0.493	0.026	−0.796	21	273
	$\cdots$, $h = 300$ km	1.159	1.476	0.048	−2.779	…	…	…	…	…	…
10	$E_c = 100$ keV, $\delta = 5$, $h = 100$ km	1.055	1.125	0.000	−0.650	1.087	0.509	0.023	−0.492	17	265
	$\cdots$, $h = 300$ km	1.129	1.302	0.256	−2.121	…	…	…	…	…	…
11	$E_c = 150$ keV, $\delta = 5$, $h = 100$ km	1.023	1.036	0.005	−0.191	1.039	0.540	0.127	−0.146	10	265
	$\cdots$, $h = 300$ km	1.089	1.188	0.191	−0.857	…	…	…	…	…	…
12	$E_c = 250$ keV, $\delta = 5$, $h = 100$ km	1.019	1.014	0.008	−0.109	1.039	0.581	0.101	−0.068	9	265
	$\cdots$, $h = 300$ km	1.052	1.102	0.082	−0.491	…	…	…	…	…	…
13	$E_c = 500$ keV, $\delta = 5$, $h = 100$ km	1.037	1.026	0.002	−0.172	1.069	0.584	0.025	−0.125	11	265
	$\cdots$, $h = 300$ km	1.038	1.110	0.069	−0.366	…	…	…	…	…	…
14	$E_c = 1000$ keV, $\delta = 5$, $h = 100$ km	1.039	1.022	0.021	−0.012	1.065	0.549	0.065	−0.005	11	265
	$\cdots$, $h = 300$ km	1.050	1.054	0.177	−0.109	…	…	…	…	…	…
15	$E_c = 3000$ keV, $\delta = 5$, $h = 100$ km	1.130	1.105	0.121	−0.008	1.346	0.260	0.126	−0.094	30	276
	$\cdots$, $h = 300$ km	1.231	1.292	0.783	−0.379	…	…	…	…	…	…

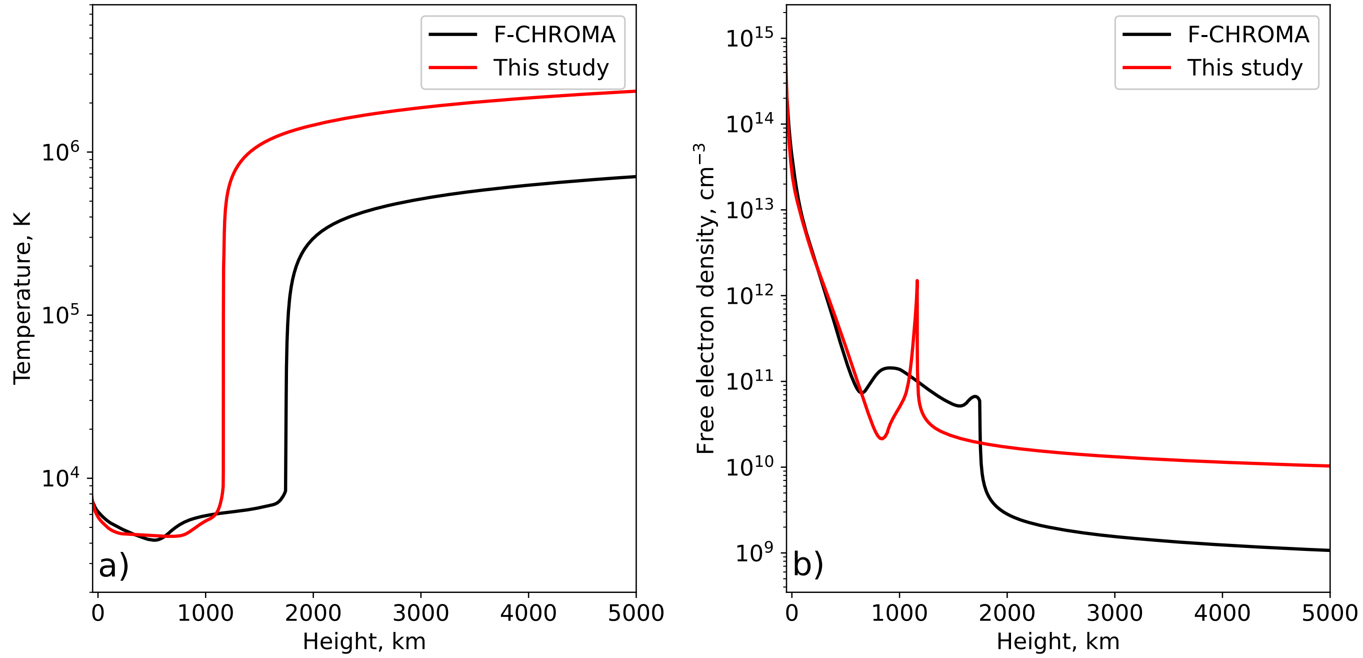

Figure 1. Comparison of the (a) temperature profiles and (b) free-electron density profiles for the initial atmospheres used for RADYN simulations in F-CHROMA grid (Carlsson et al. 2023) and in this study.

F-CHROMA grid, which is injected more gradually over a 20 s triangular pulse, and the energy flux is twice larger on average.

2.2. Modeling of Fe I 6173 Å Stokes Profiles and SDO/HMI Observables

The SDO/HMI obtains the LOS observables by measuring the Fe I 6173 Å line in two polarizations (right-circular polarization, RCP, and left-circular polarization, LCP) over six wavelength points. To model how SDO/HMI would see the flare atmospheres heated by the proton beams, we synthesize the Fe I 6173 Å Stokes profiles for the RADYN simulations using a similar approach as described in Sadykov et al. (2020). In brief, the non-LTE (NTLE) Fe atomic level populations and resulting emission from bound–bound transitions are calculated under the assumption of statistical equilibrium using the RH1.5D radiative-transfer code (Rybicki & Hummer 1991, 1992; Uitenbroek 2001; Pereira & Uitenbroek 2015). Since RH1.5D solves the statistical equilibrium equations, nonequilibrium effects are not included. The dynamic hydrogen populations and the free-electron densities are imported from the RADYN model and not recalculated, somewhat mitigating the requirement to assume statistical equilibrium in the solution of Fe I. The full Stokes profiles are solved for the Fe I 6173 Å transition, with no effects of the background polarization taken into account, and the LCP and RCP profiles are computed. The models are augmented with various settings of the imposed vertical magnetic field unchanged during the simulations. Although we consider a 500 G magnetic field setting (selected for illustration purposes only), the choice of the magnetic field does not impact the hydrodynamic simulation results, and only affects the calculations of the Stokes profiles and HMI observables. The Stokes profiles are computed from the RADYN run output, which is typically at a cadence of 0.1 s.

The properties of the Fe I 6173 Å line are computed (i) directly from the fully resolved Stokes profiles, (ii) by applying the SDO/HMI LOS pipeline to the Stokes profiles and assuming that the polarization signals are obtained instantly for every wavelength/filter, and (iii) by applying the SDO/HMI LOS pipeline to the Stokes profiles following the proper temporal sequence of polarization measurements (Schou et al. 2012). For the properties directly estimated from the fully resolved Stokes profiles, we compute the continuum intensities (calculated as the average intensity at ±1 Å from the reference wavelength of the line, $\lambda_{\mathrm{ref}} = 6173.34$ Å), line depths (defined as the strongest deviations from the continuum intensities), and line Doppler shifts (calculated using the center of gravity approach; e.g., Sadykov et al. 2019). The same observables are obtained using a simplified version of the HMI data-analysis algorithm following the original method described by Couvidat et al. (2012, 2016). The simplified pipeline is described in detail in Sadykov et al. (2020) and its application to RADYN electron-beam-heating runs is tested therein. Here, we provide a brief summary of the pipeline.

The LCP and RCP profiles of the Fe I 6173 Å are sampled in six wavelength points by assuming a Gaussian-like transmission profile in the wavelength space (with FWHM ∼ 76 mÅ). The wavelength points are centered at the rest wavelength of Fe I 6173 Å ($\lambda_{\mathrm{ref}} = 6173.34$ Å) and are sampled at 68.8 mÅ apart. From these six measurements, the first and second Fourier components are computed and used for the estimation of the HMI observables (continuum intensity, line depth, Doppler velocity, and LOS magnetic field; see Couvidat et al. 2012) with the corresponding correction factors (Couvidat et al. 2016). The Fe I 6173 Å line profile is assumed to be Gaussian. In contrast with the previous work (Sadykov et al. 2020), the line width is not assumed to be fixed but recalculated for every application of the SDO/HMI pipeline. Keeping the line width fixed and equal to the unperturbed line profile width does not change the results and conclusions qualitatively. We sample the line profiles at each time snapshot and compute "instantaneous observables" (i.e., observables where the temporal sequence of measurements is not taken into account).

The HMI LOS pipeline measurement sequence takes 45 s to be completed. Given that the heating phase lasts only 20 s, the observables will depend on the time of the heating with respect to the measurement sequence timing. In this work, for every time moment of the simulation, we assume that the SDO/HMI pipeline is centered temporally at that time moment, and compute the observables. Therefore, the dynamics of the observables presented further need to be interpreted as what "can possibly be" observed by HMI during the proton-beam-heating event rather than what "is" observed. That is, the best-case scenario is HMI happens to catch the start of the impulsive heating of a single pixel. The temporal sequence of polarizations and wavelengths are assumed following Schou et al. (2012). The polarization profiles for $t < 0$ s are assumed to be the same as the profiles of an unperturbed atmosphere at $t = 0$ s, and the same as for the $t = 100$ s time moment for any $t > 100$ s. This allows one to compute the observables during the heating phase and for the last 20 s of the run.

2.3. Results from RADYN

A summary of the strongest perturbations (both the physical properties of the atmosphere and the properties of the Fe I 6173 Å line formation and appearance) for all considered RADYN runs is presented in Tables 1 and 2. The perturbations of the atmospheric parameters are computed for heights of 100 and 300 km, which correspond to the heights where the Fe I 6173 Å line is typically formed for quiet-Sun conditions (Norton et al. 2006; Kitiashvili et al. 2015). We note here that during the flare process the Fe I 6173 Å may experience a significant chromospheric contribution (Monson et al. 2021), which we do not investigate in this work. The height of 100 km is chosen for analysis instead of 0 km because the latter is close to the bottom boundary of the modeling domain (which is just ∼60–65 km below the 0 km height) and affected by the boundary conditions. The selection of the upper height of $h = 300$ km is consistent with maximum values of $\tau_\lambda = 1$ modeled for the continuum near the Fe I 6173 Å line presented in the tables (although, as noted earlier, this does not preclude the possibility of the contribution of higher levels of the atmosphere to the Fe I 6173 Å formation). The atmospheric perturbations at $h = 300$ km for the presented runs range from several percent for the considered parameters (for moderate $E_c \sim 250$ keV values) to several tens of percent for the extremely high or extremely low values of the E_c. The perturbations are mostly several percent at the height of $h = 100$ km for these runs and rarely reach tens of percent. Vertical velocities rarely reach as much as several hundreds of meters per second at $h = 100$ km. At that height, the largest downward velocity is in Model 9 with $v_z \sim -0.794$ km s^{-1}.[11] The notation v_z hereafter corresponds to the hydrodynamic velocities in RADYN simulations. However, vertical velocities are significantly faster at a height of $h = 300$ km, where in Model 9 the peak downward velocity is $v_z \sim -2.78$ km s^{-1}. The electron-beam-induced velocities for the F-CHROMA grid were significantly lower (Sadykov et al. 2020; Monson et al. 2021). For the atmospheric parameters (temperatures, pressures, and vertical velocities at heights of $h = 100$ km and $h = 300$ km), the strongest perturbations occur for the lowest and highest values of the low-energy cutoff parameter, E_c, corresponding to the cases of the highest number of protons or the highest energy per proton, respectively.

Tables 1 and 2 also present the spectroscopic line parameters as computed from the fully resolved Stokes profiles (i.e., with no application of the SDO/HMI LOS algorithm at this point). The strongest perturbations of the Fe I line profiles (in terms of their continuum intensities, line depths, and Doppler shifts) and changes to the $\tau = 1$ heights occur in the cases of very high or very low E_c. In particular, the continuum intensity enhancement reaches more than 40% and the strongest blueshift (representing an upflow) reaches almost $v_D \sim 0.97$ km s^{-1} for Model 8 ($E_c = 3000$ keV, $\delta = 3$), which has the highest average energy per proton considered. As mentioned previously, Model 9 ($E_c = 50$ keV, $\delta = 5$) has the strongest redshift of $v_D \sim -2.78$ km s^{-1} at $h = 300$ km.

Figure 2 illustrates the maximum values of the relative continuum intensity enhancements, I_c/I_c^0, and the strongest redshift, $\min v_D$ (normally interpreted as a downflow speed, though opacity effects make a one-to-one relation difficult), as functions of the E_c and δ parameters of the proton beam energy spectrum. Hereafter, v_D corresponds to the velocities inferred from Doppler shifts of fully resolved Stokes profiles applying a center of gravity approach. While both the continuum intensity enhancement and strongest redshifts tend to increase with the change of the E_c for both δ setups, the trends for I_c/I_c^0 and v_D are slightly different. The enhancement of the continuum near the Fe I 6173 Å spectral line is in the range of 5%–10% for most of the runs and increases consistently with the increase of E_c. The situation is the opposite for Doppler shifts, where the strongest redshifts tend to increase with the decrease of E_c.

Among the considered models, two are of special interest. Model 8 has the strongest enhancement of the continuum intensity near the line, and Model 9 has the strongest perturbation of the Doppler shift v_D of the line profile. Therefore, both models are chosen for more detailed analysis. Figure 3 displays the evolution of the temperature and pressure relative to their unperturbed values (at $t = 0$ s) and the vertical velocities for these two models. One can see that both models resulted in significant perturbations of the lower atmosphere. Figure 4 visualizes the behavior of temperature, vertical velocity, gas pressure, and the $\tau = 1$ height of the Fe I 6173 Å line core and nearby continuum as a function of time. Model 8 has a stronger temperature response and a larger change in the $\tau = 1$ heights than does Model 9. In Model 9, during the time interval of ≈30–90 s, there is extensive enhanced pressure in the region of line formation that is not evident in Model 8. In contrast to Figure 3(e), Figure 3(b) shows the downward propagation of the pressure enhancement peak in the lower atmosphere, below 750 km. In contrast, for Model 8 the increase of the gas pressure happens during the first 20 s of the run during the heating phase.

2.4. Analysis of Stokes Profiles

Figures 5 and 6 illustrate the evolution of the Fe I 6173 Å LCP and RCP profiles throughout the simulation. Overall, the line profiles presented in Figure 5 (corresponding to Model 9) do not experience notable changes until after the initial heating phase, when they become asymmetric: The blue wing of the profiles deepens between $t \approx 20$ and 30 s and then enhances, with the strongest enhancement happening at around $t \sim 60$ s. Figure 4(b) demonstrates that the strongest enhancement of the blue wing follows the strongest downward motions of the atmosphere at $h = 300$ km by just several seconds. In contrast to that behavior, the dynamics in Model 8 result in more

---

[11] Here, we define negative velocities as downflows and positive velocities as upflows.

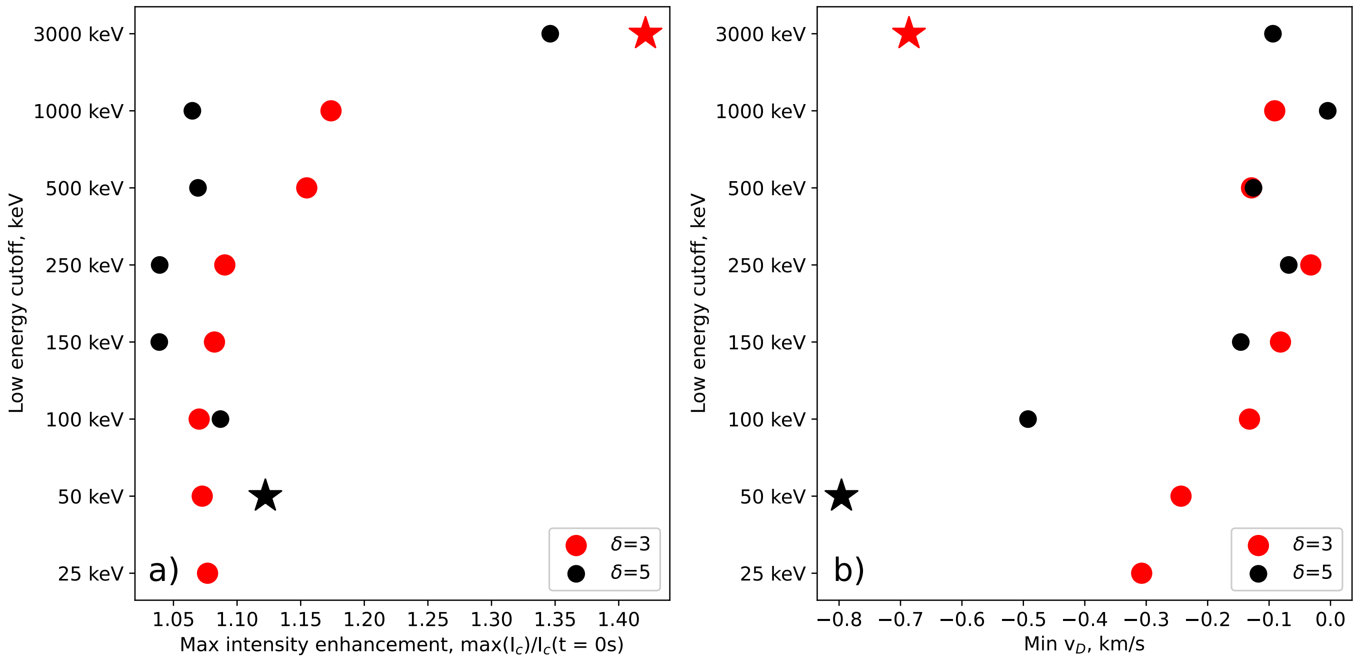

Figure 2. The maximum intensity enhancement (a) and the strongest Doppler redshift (b) as a function of the low-energy cutoff, E_c, for the considered models. The visualization is based on the RADYN model summaries in Tables 1 and 2. The models selected for the detailed analysis (Model 8, $E_c = 3000$ keV, $\delta = 3$, $F_d = 10^{11}$ erg cm^{-2} s^{-1}; and Model 9, $E_c = 50$ keV, $\delta = 5$, $F_d = 10^{11}$ erg cm^{-2} s^{-1}) are marked by asterisks.

enhanced, complex shapes of the line profiles during the heating phase and right after it, as seen in Figures 6(a)–(c). In particular, the Fe I line LCP and RCP profiles demonstrate an emission feature superimposed with the absorption and have an enhanced blue wing after 10 s of the start of the run. The enhancement of the Fe I polarization profiles is also reflected in $\tau = 1$ heights: The heights lie in a more shallow region, within $h \sim 50$–200 km (see Figure 4(h)).

In addition to properties derived directly from the LCP and RCP profiles, we have applied the simplified SDO/HMI pipeline (Sadykov et al. 2020; also described in Section 2.2) and computed the instantaneous and time-dependent LOS observables. The results are presented in Figure 7 for the case of a 500 G imposed vertical magnetic field, and do not change qualitatively for other values of the field. The instantaneous observables demonstrate the same patterns as the spectral line properties (continuum intensities near the line, line depths, and Doppler shifts) derived from the full-resolution line profiles for Models 8 and 9. The systematic offset of the synthetic observables with respect to the quantities derived from their full-resolution counterparts is typically a result of the non-Gaussian shape of the Fe I line (see Figures 5 and 6) while the SDO/HMI LOS pipeline relies on the Gaussian-shape assumption (Couvidat et al. 2016). The behavior of the time-dependent observables (taking into account the timing of the polarization measurements at different wavelengths) is close to the instantaneous observables for Model 9 (Figures 7(a)–(d)). However, for Model 8 the behavior of the line depth (Figure 7(f)) and Doppler velocity (Figure 7(g)) observables differ dramatically. In particular, while the redshifts measured from the fully resolved LCP and RCP profiles reach only ≈ -0.7 km s^{-1}, the time-dependent SDO/HMI observables demonstrate Doppler shifts greater than -2 km s^{-1}. The vertical magnetic field observable fluctuates for this model approximately in the range of 300–900 G, while its true value was always unchanged and equal to 500 G. Such dynamics are due to the strong impulsive heating whose duration (20 s) is less than the duration of the SDO/HMI LOS pipeline procedure (45 s). Model 9 (Figures 7(a)–(d)) shows a much better agreement between the properties of the line profile derived directly from the spectrum and the SDO/HMI observables with respect to Model 8 (Figures 7(e)–(h)), most likely because of the more gradual evolution of the Fe I polarization profiles evident in Figures 5 and 6. Overall, it once again confirms that SDO/HMI LOS observables, including a continuum intensity observable, have to be interpreted with caution during solar flares (Švanda et al. 2018).

3. 3D Acoustic Models Driven by RADYN Simulations

In this section, we use the atmospheric response to proton beam heating—as computed by RADYN—as an input to an acoustic model to measure the amplitude of helioseismic waves that may be generated. We provide a brief description of the acoustic model and the coupling procedure for the RADYN output in Section 3.1, followed by the results of this modeling in Section 3.2.

3.1. Model Description

The 3D acoustic model treats acoustic oscillations as linear, adiabatic perturbations to pressure, density, and velocity (Stefan & Kosovichev 2020). The background stratification for the solar interior is derived from the Standard solar model (Christensen-Dalsgaard et al. 1996), which smoothly transitions to the atmosphere used in the RADYN simulations. The transition location in the Standard solar model, at $R = 695.707$ Mm relative to the solar center, is chosen where the mass density is equal to that at $z = 0$ km in the RADYN mesh.

The computational acoustic model itself is semi-spectral, with the radial derivatives evaluated numerically and polar- and azimuthal-angle derivatives evaluated spectrally using spherical harmonics. While the acoustic model does not include

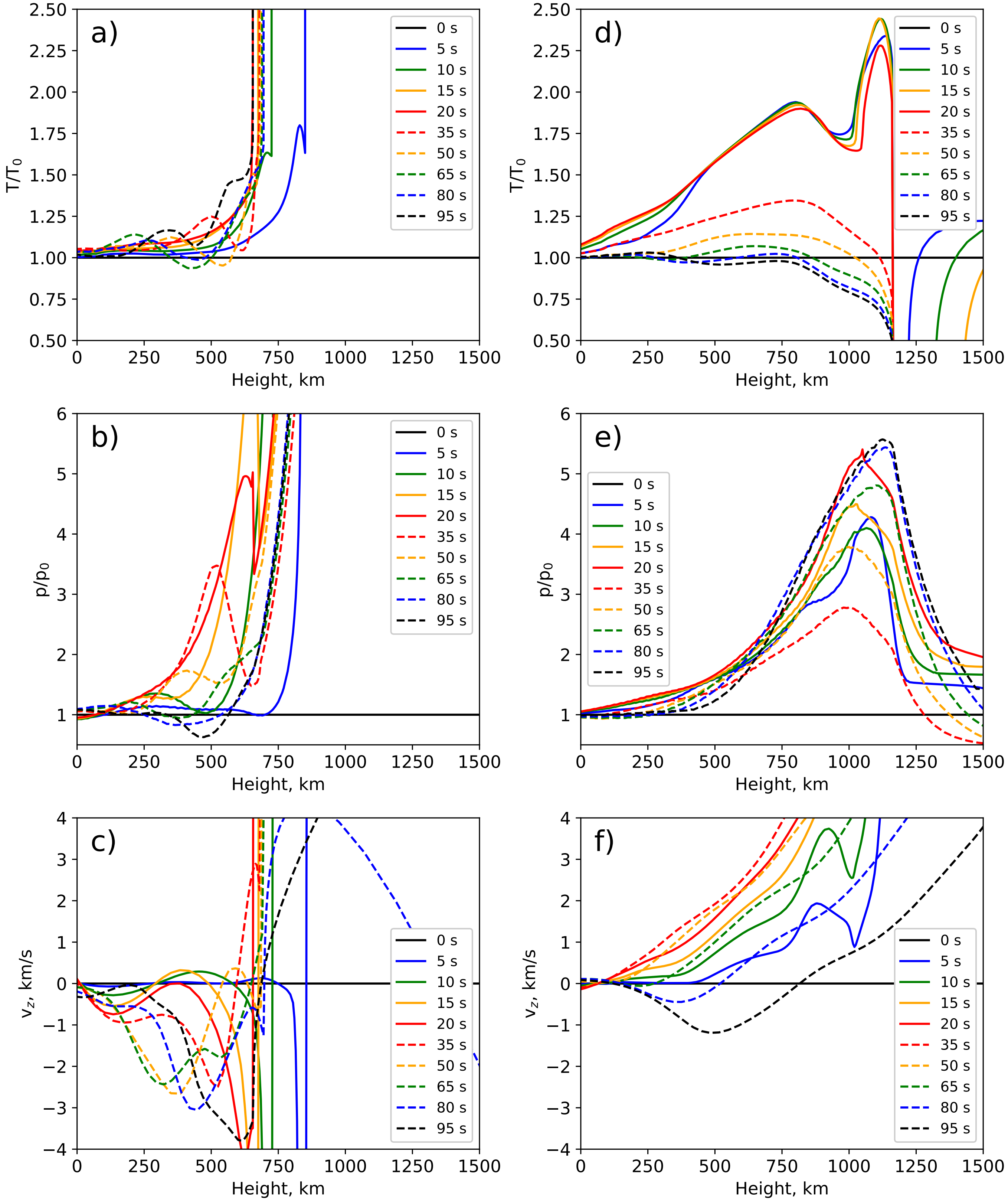

Figure 3. Evolution of the temperature enhancement relative to $t = 0$ s moment (a), gas-pressure enhancement relative to $t = 0$ s moment (b), and vertical velocity (c) at the different time moments for RADYN Model 9 ($E_c = 50$ keV, $\delta = 5$, $F_d = 10^{11}$ erg cm^{-2} s^{-1}). Panels (d)–(f) show the same parameters as in panels (a)–(c) but for the RADYN Model 8 ($E_c = 3000$ keV, $\delta = 3$, $F_d = 10^{11}$ erg cm^{-2} s^{-1}).

radiative damping, the generated oscillations are damped according to the horizontal wavenumber, with damping parameters derived from quiet-Sun pressure wave (*p*-mode) data reported by Rhodes et al. (2011). We consider the choice of quiet-Sun damping parameters, as opposed to active-region-like, appropriate here as the majority of the sunquake wave front propagates outside the generating active region, where the magnetic field is moderate or weak.

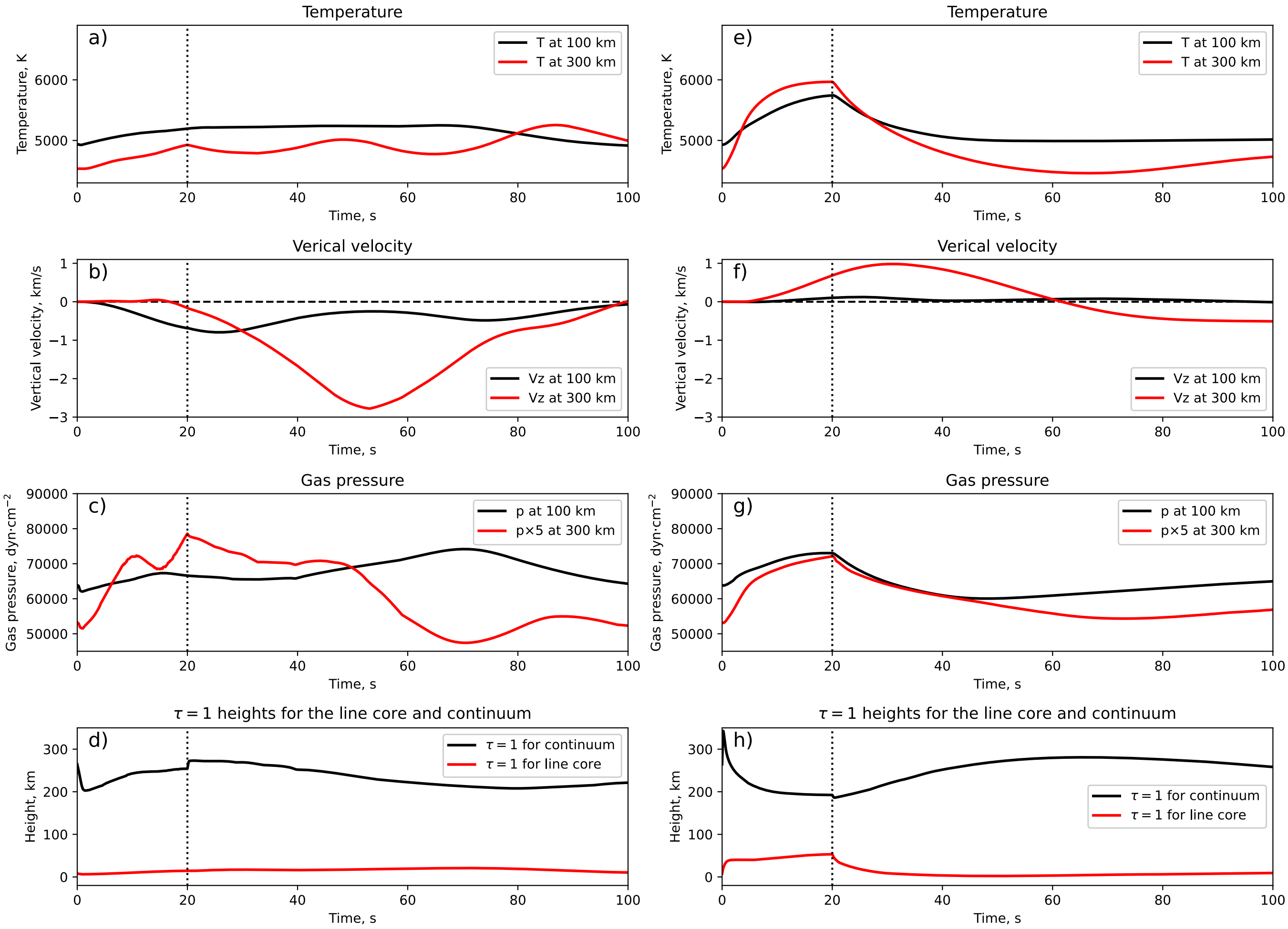

Figure 4. Illustration of the temperature (a), vertical velocity v_z (b), and gas pressure (c) as a function of time at heights of 100 km (black solid curve) and 300 km (red solid curve) for RADYN Model 9 ($E_c = 50$ keV, $\delta = 5$, $F_d = 10^{11}$ erg cm^{-2} s^{-1}). The $\tau = 1$ heights for the Fe I 6173 Å line core and continuum are presented in panel (d). Panels (e)–(h) show the same parameters as in panels (a)–(d) but for the RADYN Model 8 ($E_c = 3000$ keV, $\delta = 3$, $F_d = 10^{11}$ erg cm^{-2} s^{-1}).

We take advantage of the advanced treatment of radiation in RADYN by deriving our acoustic model input using the simulated perturbations to gas pressure. These gas pressure perturbations are smaller in RADYN than they would be in the acoustic model as RADYN accounts for the energy lost in optically thin and NLTE optically thick radiation. Here, gradients in the gas pressure determine the acceleration a plasma parcel experiences from the supplied heating, and the input accelerations are computed from the RADYN simulations with $\dot{v_r} = (1/\rho_0) \cdot \partial P'/\partial r$, where ρ_0 is the initial state's mass density. An example of the input acceleration profiles, as described in the next section, for low-energy cutoffs $E_c = 50$ keV and $E_c = 3000$ keV (Models 9 and 15) interpolated onto the hydrodynamic model's background mesh is shown in Figure 8. We highlight these models in particular as they span the two extremes of our low-energy cutoff parameter space.

We assume a constant cross-sectional area, and the horizontal profile of the input accelerations is considered to be Gaussian with a FWHM of 1500 km. The FWHM is based on HMI observations of sunquake kernels that range in size from one to several pixels; this corresponds to an impact site between 750 and 2000 km. Where the lower end of the supplied accelerations ends, slightly below $R = 695.707$ Mm, the functions are appended by a Gaussian with a drop-off closely matching the unappended input. A similar drop-off is applied to the upper end of the supplied accelerations, which extend to the top of the modeled corona, to avoid boundary effects that may be caused by providing input close to the upper boundary. The Gaussian upper drop-off begins 350 km from the upper boundary with a FWHM of 125 km. An additional description of the acoustic model, including numerics, is provided in Stefan & Kosovichev (2020).

3.2. Results from the Acoustic Model

We are primarily interested in the behavior of the photospheric radial velocity, as this is generally the largest component of the LOS velocity in SDO/HMI Dopplergrams for observations close to the disk center. We then examine the resulting photospheric *p*-mode wave front, with absolute maximum radial velocity for each case shown as a function of horizontal distance from the beam target in Figure 9. Note that acoustic-gravity waves—not typically observed in actual sunquake events—are generated in addition to the usual *p*-mode wave front. In the cases where the cutoff energy is greater than 250 keV, these acoustic-gravity waves have amplitudes that exceed the *p*-mode wave front. We therefore examine the absolute maximum amplitude at each distance within 5 minutes of the wave front travel time predicted by ray

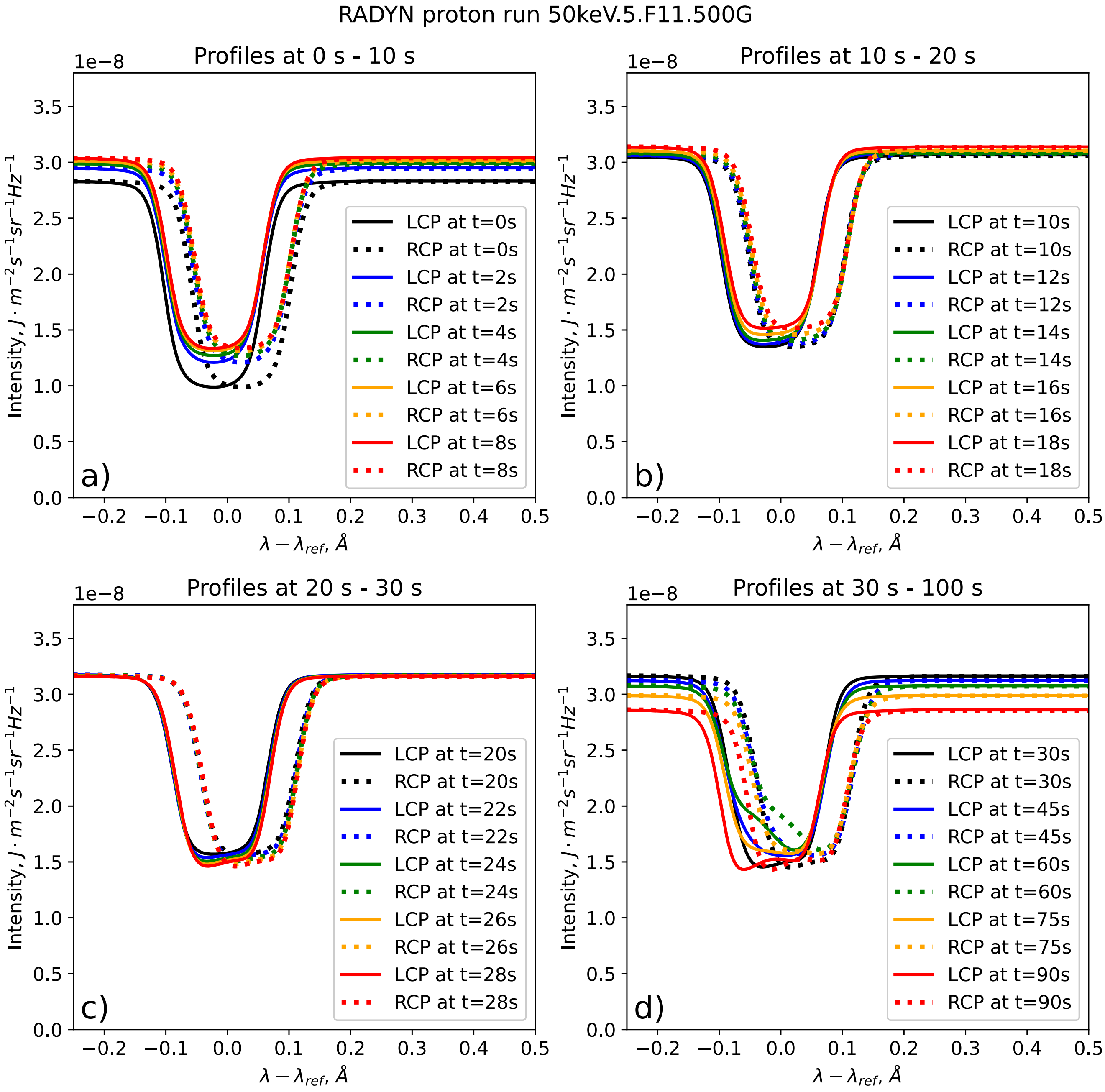

Figure 5. Fe I 6173 Å LCP (solid) and RCP (dashed) line profiles for Model 9 ($E_c = 50$ keV, $\delta = 5$, $F_d = 10^{11}$ erg cm^{-2} s^{-1}) with 500 G imposed vertical magnetic field at 0–10 s (a), 10–20 s (b), 20–30 s (c), and 30–100 s (d) of the run. The times at which the profiles are sampled are coded by color, $\lambda_{\rm ref} = 6173.34$ Å.

theory; however, it is not possible to disentangle the two wave fronts for short (<5–7 Mm) distances.

We observe core velocities in the acoustic model which are significantly greater than those in the RADYN simulations, in particular for the simulations with low cutoff energies. For example, the acoustic model predicts a magnitude of the radial velocity for Model 9 ($E_c = 50$ keV, $\delta = 5$) of 68.7 km s^{-1}; in such cases, we do not expect the predictions that are close to the source to be reliable because of both the linear nature of the model and the lack of radiative damping. Conversely, the magnitude of the radial velocity for Model 15 ($E_c = 3000$ keV, $\delta = 5$) at the beam core is only 0.751 km s^{-1}, which securely falls in the linear regime. Thus, we consider the entire range of the acoustic model to be reliable for the higher-cutoff-energy cases.

The relationship between the absolute maximum radial velocities of each case remains largely the same over distance as compared to the beam core. In general, the greatest absolute velocities are associated with small low-energy cutoffs, with the wave front amplitudes decreasing with increasing low-energy cutoff. There is relatively little deviation in this relationship when increasing the spectral index from $\delta = 3$ to $\delta = 5$, though we note that the radial velocities for the $E_c = 500$ keV cases do change appreciably from the $\delta = 3$ case (Model 6) to $\delta = 5$ case (Model 13). In the associated acceleration profile from each model, we observe significantly stronger evaporation in the $\delta = 5$ case as well as a downward-propagating acceleration front that penetrates slightly more deeply in Model 13 than in Model 6. While the initial evaporation in each case is similarly impulsive—that is, the

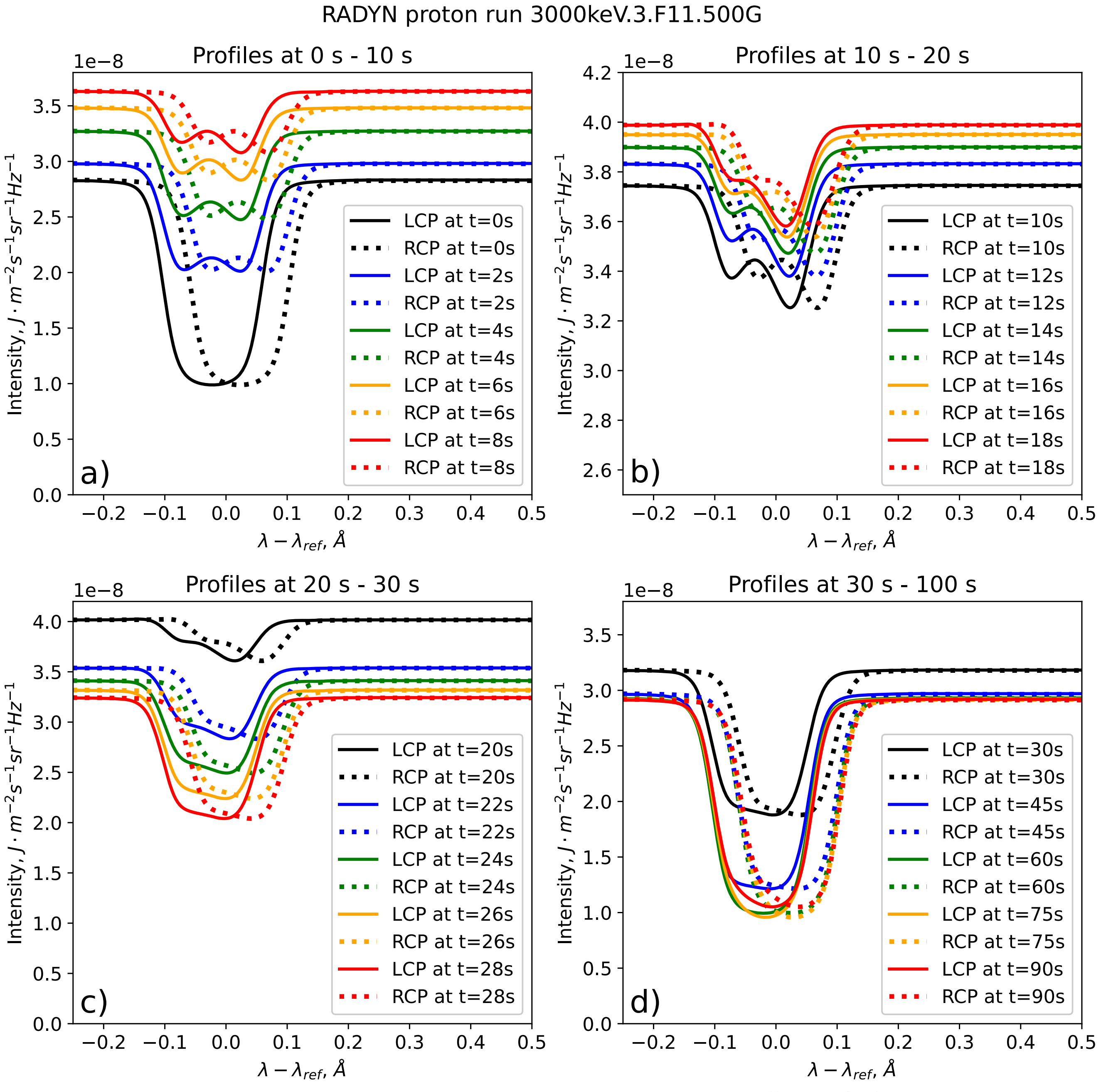

Figure 6. Same as Figure 5 but for Model 8 ($E_c = 3000$ keV, $\delta = 3$, $F_d = 10^{11}$ erg cm^{-2} s^{-1}).

evaporation fronts propagate upwards with similar speeds—more of the beam energy is released in the initial evaporation of Model 13. For models with lower-energy cutoffs, there is a similar increase in acceleration magnitude when moving from $\delta = 3$ to $\delta = 5$. The downward-propagating acceleration front is weak for low-energy cutoff $E_c = 1000$ keV (Models 7 and 14) and nonexistent for low-energy cutoff $E_c = 3000$ keV (Models 8 and 15), and the radial velocity in these two cases changes the least with spectral index. The lack of the downward-propagating front in Model 15 is clearly seen in the comparison with Model 9 in Figure 8.

We now look more closely at the maximum radial velocity at a horizontal distance of $X = 18$ Mm, indicated by the vertical dashed line in Figure 9, where the sunquake wave front is expected to reach its maximum amplitude (aside from the beam core), based on observations (see Figure 3(d) in Macrae et al. 2018; Figure 7 in Zharkov et al. 2020; and Figure 2 in Sharykin & Kosovichev 2020). Explicitly plotting these velocities on a log–log scale, as in Figure 10, we find that the generated sunquakes fall into two separate regimes. There is a low-energy cutoff regime extending up to $E_c = 250$ keV where the sunquake amplitudes are similar to observations (on the order of hundreds of meters per second), and a high-energy cutoff regime beginning at $E_c = 1000$ keV where the sunquake amplitude is significantly lower than in observations.

4. Summary and Discussion

To summarize the results, we claim that there are two regimes found in which the perturbations of the line profiles and the atmosphere were significant and resulted in a potential helioseismic response and/or a white-light flare (see Figure 2). We have selected two models, the one with the strongest

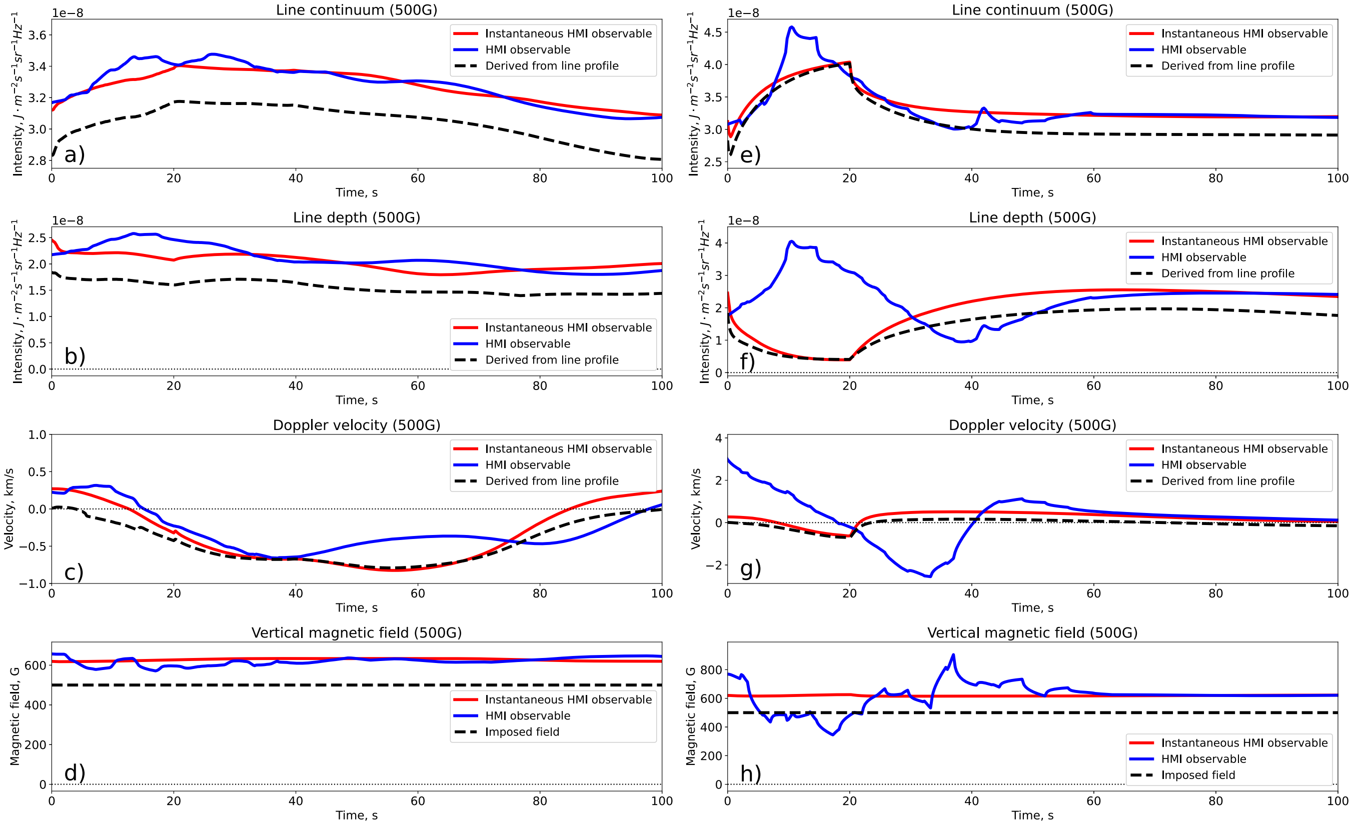

Figure 7. The continuum intensity (a), line depth (b), Doppler velocity (c), and magnetic field (d) inferred from the synthetic Fe I 6173 Å line profiles from Model 9 with an imposed vertical uniform 500 G magnetic field. The black dashed curves correspond to measurements inferred from the synthetic line profiles computed using RH code (noted as v_D in the text). The red solid curves show "instantaneous" observables obtained with the HMI algorithm applied to instantaneous line profiles. The blue curves show the observables obtained with the HMI algorithm applied with the actual observing sequence timing centered at the reference time. The black dotted–dashed horizontal lines mark the zero level of the observables. Panels (e)–(h) illustrate the same quantities for Model 8.

enhancement of the continuum near the line (Model 8; $E_c = 3000$ keV, $\delta = 3$, $F_d = 10^{11}$ erg cm^{-2} s^{-1}), and the one with the strongest Doppler shift v_D (Model 9; $E_c = 50$ keV, $\delta = 5$, $F_d = 10^{11}$ erg cm^{-2} s^{-1}). Model 9 causes gradual but strong changes in the atmospheric parameters, resulting in a ≈12% increase in flare continuum during the heating phase. The Doppler velocity derived from fully resolved polarization profiles has the strongest redshift of $v_D \sim -0.8$ km s^{-1} about 40 s after the heating. The SDO/HMI observables, in general, closely follow the properties of the full-resolution line profile. The other model, Model 8, causes a much stronger enhancement of the continuum near the Fe I 6173 Å line (of the order of 42%) with respect to Model 9 and also results in the Fe I 6173 Å redshifts of $v_D \sim -0.7$ km s^{-1} at the end of the heating phase. The SDO/HMI observables in this model differ significantly from the counterparts derived from the full-resolution line profiles. Overall, both models demonstrate the impact on the deep layers of the solar atmosphere, and the hydrodynamic velocity analysis and spectral analysis of the Fe I 6173 Å line do not yet allow us to claim whether the proton beams of high energy per proton or low energy per proton are the preferential candidates for causing sunquakes. To provide more insights, we utilize the responses of the atmosphere to the proton beam heating and impose this response into the 3D acoustic models (Section 3). While the Doppler velocities in the RADYN models do not differ much at either extreme of the low-energy cutoff, the physical velocities in the acoustic model are significantly stronger for Model 9 ($E_c = 50$ keV, $\delta = 5$, $F_d = 10^{11}$ erg cm^{-2} s^{-1}) than for Model 8. The continuum intensity enhancement derived from the RADYN simulation is, on the contrary, stronger for the $\delta = 3$ cases, with Model 8 producing the strongest enhancement. Overall, we show not only that sunquakes can be generated from a high injected flux of protons with relatively low cutoff energy, but that these sunquakes have much higher amplitudes than those predicted from simulations with large cutoff energies. This is particularly significant as large low-energy cutoffs are more difficult to physically justify.

The role of proton beams in the solar flare energy deposition has been discussed for more than five decades (Švestka 1970; Simnett 1986), yet without a clear understanding of the energy fraction carried by these beams. Some works (Emslie et al. 2012) suggest that the energy transported by the proton beams in solar flares is comparable to that of the electron beams. Proton beams are an attractive candidate as a mechanism to explain sunquake excitation as they deposit energy significantly deeper in the solar atmosphere than electron beams. To investigate the possible reasons behind the sunquake generation, we notice here that the proton beams also carry more momentum with respect to the electron beams of similar energy due to the difference in the particle masses. Given that the energy spectrum of the proton beam is determined by the power law,

$$\frac{dN}{dE} = \begin{cases} AE^{-\delta}, & E \geqslant E_c \\ 0, & E < E_c \end{cases}, \tag{1}$$

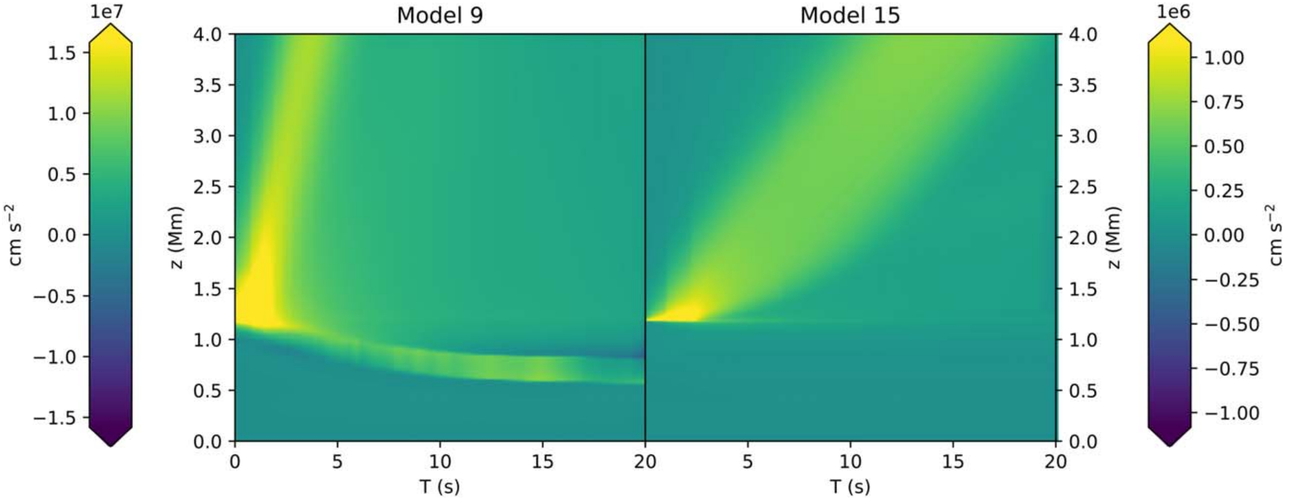

Figure 8. Time-dependent acceleration profiles derived from the RADYN proton beam simulations for Models 9 (left) and 15 (right).

with the constant A found by normalizing to the known deposited energy rate,

$$F_d = \int_{E_c}^{\infty} E\frac{dN}{dE}dE \quad \Rightarrow \quad A = F_d\frac{\delta - 2}{E_c^{-\delta+2}}, \tag{2}$$

the total momentum flux of the beam (in the nonrelativistic limit) and the average energy per particle are then

$$M_d = \int_{E_c}^{\infty} \sqrt{2m_p E}\frac{dN}{dE}dE = \sqrt{2m_p F_d}\frac{\delta - 2}{\delta - \frac{3}{2}}\sqrt{\frac{F_d}{E_c}} \tag{3}$$

and

$$\langle E_p \rangle = \frac{F_d}{\int_{E_c}^{\infty}\frac{dN}{dE}dE} = \frac{\delta - 1}{\delta - 2}E_c. \tag{4}$$

Although we do not analyze the momentum transport in detail in this work, it is helpful to provide some estimates. The injected momentum flux for the proton beam in Model 9 (with $F_d = 10^{11}$ erg cm^{-2} s^{-1}, $\delta = 5$, and $E_c = 50$ keV) is $M_d \sim 5.5 \times 10^2$ g cm^{-1} s^{-2}. The total momentum deposited per unit area during 20 s therefore is $M_d^{\rm tot} = M_d \Delta t \sim 1.1 \times 10^4$ g cm^{-1} s^{-1}. Assuming the photospheric density $\rho \approx 10^{-7}$–10^{-8} g cm^{-3} (considering the quiet Sun and sunspot model atmospheres, correspondingly; Allred et al. 2015) and the characteristic scale height of $H \approx 100$ km, the bulk velocity of the plasma is $v \approx M_d^{\rm tot}/(\rho H) \approx 0.1$–$1$ km s^{-1}. The latter velocity estimate is comparable to what is expected for sunquakes, and we can therefore conclude that the momentum transport by the proton beams may play an important role in sunquake initiation.

We have explored whether proton beams of the deposited energy flux ($F_d = 10^{11}$ erg cm^{-2} s^{-1}) are capable of exciting sunquakes with amplitudes similar to observations. Depending on the frequency filtering applied to Dopplergram observations, the observed range of sunquake amplitudes measured in the LOS velocity is 50–200 m s^{-1} (Sharykin & Kosovichev 2020; Zharkov et al. 2020). This LOS velocity is composed mainly of the radial component—reported here in Section 3.2—when the sunquake occurs close to the disk center. When the event occurs closer to the limb, however, the contribution from the tangential component of velocity increases; the tangential component, in general, is out of phase with the radial component and may decrease the observed sunquake amplitude at intermediate locations on the disk. For fixed cutoff energy, we find that the beam with spectral index $\delta = 5$ produces a higher-amplitude wave front than the corresponding $\delta = 3$ beam in nearly every case; the only outlier here is $E_c = 3000$ keV, though the difference is at most only 0.5 m s^{-1}. This is generally consistent with Equation (3), which shows that, given the same E_c and F_d, larger values of δ result in larger momenta. Also, the momentum flux for fixed cutoff energy varies weakly with the spectral index, $M_d \propto (\delta - 2)\big/(\delta - \frac{3}{2})$, and is only significant for smaller values of δ. For example, a proton beam with $\delta = 7$ is expected to deposit only 6% more momentum than the same beam with $\delta = 5$. However, for the considered $\delta = 3$ and $\delta = 5$, the difference in M_d for the beams with the same E_c is nearly 29%.

The momentum is also inversely proportional to the $\sqrt{E_c}$, which explains the increasing trend of the Doppler velocities in Figure 2(b). Decreasing the cutoff energy has a similar effect on the energy spectrum of the proton beam as increasing the spectral index, though the momentum flux depends more strongly on the cutoff energy, $M \propto 1\big/\sqrt{E_c}$. This dependence is only noticeable for $E_c \geqslant 250$ keV; for cutoff energies less than this, the decrease in sunquake amplitude with increasing cutoff energy is much milder. This weak dependence on cutoff energy in the lower end of the parameter space is measurable in principle by HMI with its precision of 13 m s^{-1} at disk center (Schou et al. 2012), though in practice the addition of the background convective noise would make this difference very difficult to measure. Furthermore, different input beam energy fluxes in observed sunquakes may further convolute the amplitude discrepancy.

The F-CHROMA models considered in Sadykov et al. (2020) have a peak energy deposition rate of $F_d = 10^{11}$ erg cm^{-2} s^{-1}. However, the average energy deposition rate was twice lower than that value, which may impact the close comparison of F-CHROMA models and the RADYN proton-beam-heating models considered in this work. Figure 11 illustrates a comparison of the response of the atmospheric parameters at $h = 300$ km for the proton beam model with $F_d = 10^{11}$ erg cm^{-2} s^{-1}, $E_c = 50$ keV, and $\delta = 5$ (Model 9) and the electron-beam-heating model with $F_d = 10^{11}$ erg cm^{-2} s^{-1}, $E_c = 15$ keV, and $\delta = 5$ from Graham et al. (2020). The RADYN electron-beam-heating model had a duration of

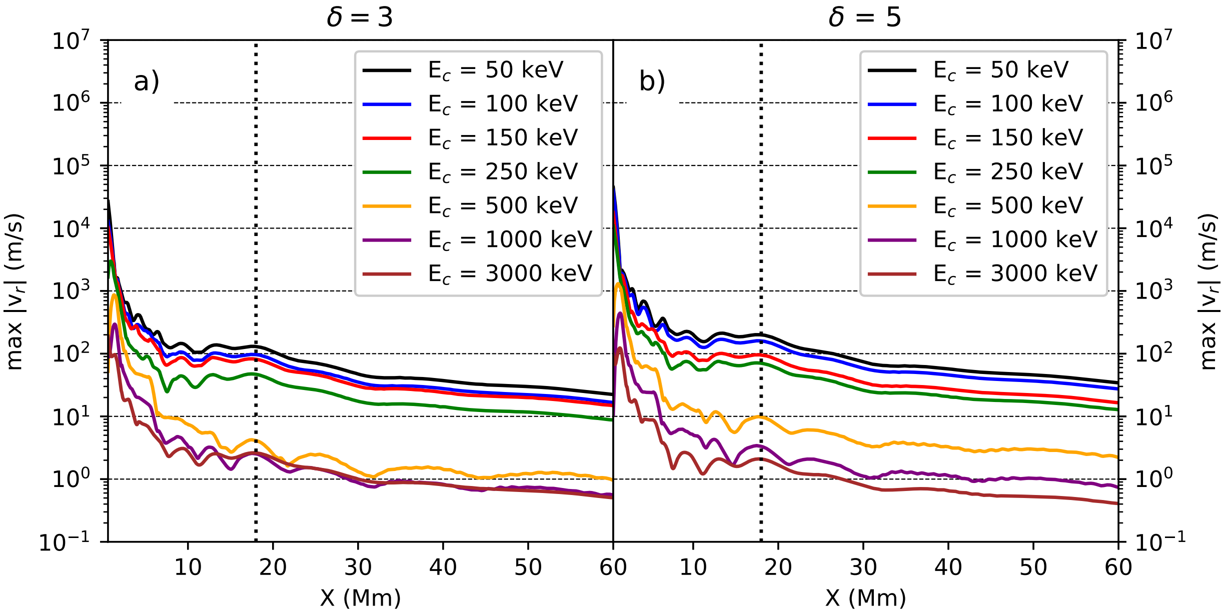

Figure 9. Log of the respective sunquake wave front amplitudes as a function of distance from the excitation source. The typical *p*-mode wave front is isolated from other waves generated in the acoustic model by considering the maximum amplitude only within 5 minutes of the predicted wave front arrival time. The sample of velocities presented in Figure 10 is marked by the vertical dashed line.

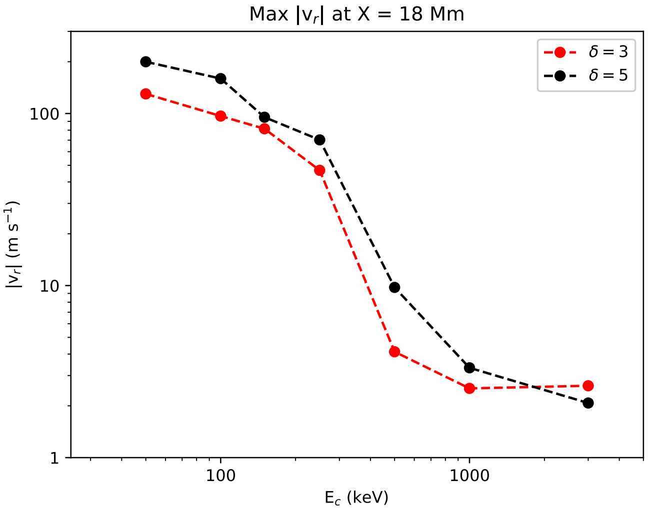

Figure 10. The sunquake wave front amplitude at $X = 18$ Mm for cutoff energies $E_c = 50$ keV to $E_c = 3000$ keV, with $\delta = 3$ in red and $\delta = 5$ in black.

heating of 20 s, similar to the one in the proton models, and a total duration of the run of 60 s. One can see in Figures 11(a)–(c) that, while experiencing weaker but still comparable temperature enhancement, the electron-beam-heating model does not result in strong downward velocities and pressure enhancements at $h = 300$ km. The dynamics of the atmospheres for the considered models are presented in more detail in Figures 11(d)–(l). While we do not perform a detailed study of the atmospheric dynamics in this work, it is worth noting that the behavior of the atmosphere heated by the beam with a large $E_c = 3000$ keV (Model 8) differs dramatically from the behavior of the atmosphere heated by the beam with a small $E_c = 50$ keV (Model 9), as well as from the considered electron-beam-heating case.

The correlation of the white-light emission (including SDO/HMI observable continuum) with the hard X-ray sources in solar flares (Battaglia & Kontar 2012; Watanabe & Imada 2020) suggests that the electron beam heating and radiative back-warming can enhance the white-light emission. Figure 2(a) demonstrates that proton beams can contribute to the enhancements of the continuum near the Fe I 6173 Å line as well. The figure also shows a tendency of the white-light enhancements to increase with the increase of E_c and preferring lower δ values. This is in qualitative agreement with Equation (4), which demonstrates that (i) for the same E_c the $\delta = 3$ beam particles have, on average, 50% more energy per particle, and (ii) the $\langle E_p \rangle$ is directly proportional to E_c. The higher values of $\langle E_p \rangle$ would indicate that the proton beam particles, on average, have to encounter thicker media to lose their energy through thermalization and, therefore, have to penetrate deeper into the solar atmosphere. All of the considered proton beam models exceeded this enhancement: 3.9% was the weakest enhancement value observed for Models 11 and 12, Models 6–9 and 15 had an enhancement of more than 10%, and the remaining model enhancements were concentrated within the 6%–10% range. It is also important to note that the enhancements reported in this work are derived directly from the computed continua near the Fe I 6173 Å line and not after applying the SDO/HMI observable algorithm, which can potentially generate artificial enhancements of the continua (Mravcová & Švanda 2017; Švanda et al. 2018).

For the models considered in this work, we have found two separate regimes in the low-energy cutoff spectrum for the proton beams: Small E_c beams which produce a strong seismic signal, and large E_c beams which produce comparatively more intense continuum emission. Observational evidence for such a duality can be found in, for example, the analysis of Pedram & Matthews (2012), where white-light enhancement for a sample of nine flares was found to be noticeably weaker in sunquake-generating events. However, first, both the RADYN model and acoustic model show an increase in the Doppler velocity and physical velocity, respectively, in the $E_c = 3000$ keV beam when the spectral index steepens from $\delta = 5$ to $\delta = 3$. It is possible that such large low-energy cutoffs can explain sunquake-generating events with significant white-light

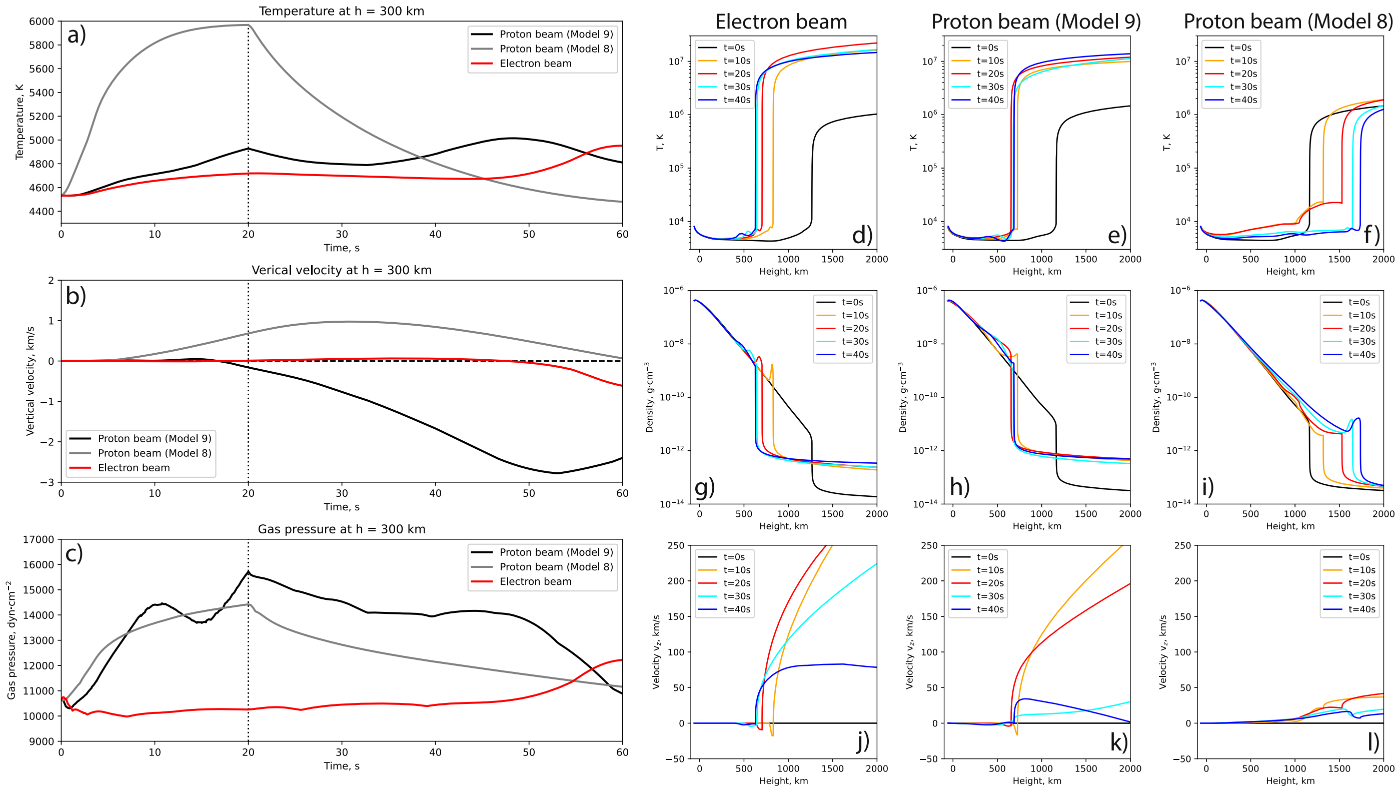

Figure 11. Illustration of the temperature (a), vertical velocity v_z (b), and gas pressure (c) as a function of time at a height of 300 km for Model 9 (black line), Model 8 (gray line), and for a RADYN simulation of nonthermal electron beam heating characterized by a power law with $E_c = 15$ keV, $\delta = 5$, $F_d = 10^{11}$ erg cm^{-2} s^{-1} (considered in Graham et al. 2020, red line). Panels (d)–(f) highlight the evolution of the temperature profiles for these models, panels (g)–(i) densities, and panels (j)–(l) vertical velocities.

enhancement, though an extension of this analysis to higher low-energy cutoffs and lower spectral indices is necessary to verify the trend. Second, the Fe I 6173 Å line profiles for Model 9 that resulted in a strong helioseismic response in 3D acoustic simulations (see Figure 5) disagree with the observations by SDO/HMI of at least some sunquake events. Specifically, the filtergrams presented by Sharykin & Kosovichev (2020, see their Figure 3(b)) and, more recently, by Kosovichev et al. (2023, see their Figure 10) demonstrate that the absorption feature of the Fe I 6173 Å line almost disappears at the location of the sunquake photospheric source. Such behavior qualitatively agrees with the profiles synthesized for Model 8 (see Figure 6) but not for Model 9. Given that weaker F-CHROMA electron beams are found to suppress the Fe I 6173 Å line absorption feature by ∼30% (see Figure 2 in Sadykov et al. 2020), the consideration of the impact by both the proton and electron beams together on the atmosphere may be necessary to explain the line profile dynamics.

A population of the very-high-energy (>30 MeV) protons can be diagnosed by producing the 2.223 MeV neutron-capture γ-ray line (Shih et al. 2009). However, the lower-energy proton distribution is currently almost "invisible" to the observer. Recently, Kerr et al. (2023) studied the Orrall–Zirker effect (Orrall & Zirker 1976) by performing proton-beam-driven RADYN simulations, with $F_d = 10^9$–10^{11} erg cm^{-2} s^{-1}, $E_c = 150$ keV, and $\delta = 5$. Though their models predicted a much weaker, and very transient, signal than earlier experiments suggested, Kerr et al. (2023) did find a detectable nonthermal enhancement of Lyman lines produced via a charge exchange between the protons in the beam and the ambient plasma, and indicated the potential possibility to diagnose the injected beam via Lyβ observations from the Spectral Imaging of the Coronal Environment instrument on board the Solar Orbiter. Figure 4 of Orrall & Zirker (1976) also indicates that the enhancements of the Lyα wings are most notable for lower δ values and for the ≈30 keV protons (also noticed in Simnett 1995). This provides an opportunity to observationally test the modeling-based selection rule that lower-energy proton beams are responsible for sunquakes, especially given that many strong flares have helioseismic counterparts (Sharykin & Kosovichev 2020).

Acknowledgments

This research was supported by NSF grant Nos. 1916509 and 1835958 and NASA grant Nos. NNX14AB68G and NNX16AP05H. V.M.S. acknowledges the NSF FDSS grant No. 1936361. G.S.K. acknowledges the financial support from a NASA Early Career Investigator Program award (grant No. 80NSSC21K0460). J.C.A. acknowledges funding from the Heliophysics Innovation Fund of the ISFM program and from the Heliophysics Supporting Research Program. A.F.K. acknowledges the NSF grant No. 1916511.

ORCID iDs

Viacheslav M. Sadykov https://orcid.org/0000-0002-4001-1295
John T. Stefan https://orcid.org/0000-0002-5519-8291
Alexander G. Kosovichev https://orcid.org/0000-0003-0364-4883
Andrey M. Stejko https://orcid.org/0000-0001-7483-3257
Adam F. Kowalski https://orcid.org/0000-0001-7458-1176

Joel C. Allred https://orcid.org/0000-0003-4227-6809
Graham S. Kerr https://orcid.org/0000-0001-5316-914X

References

Abbett, W. P., & Hawley, S. L. 1999, ApJ, 521, 906
Allred, J. C., Alaoui, M., Kowalski, A. F., & Kerr, G. S. 2020, ApJ, 902, 16
Allred, J. C., Hawley, S. L., Abbett, W. P., & Carlsson, M. 2005, ApJ, 630, 573
Allred, J. C., Kowalski, A. F., & Carlsson, M. 2015, ApJ, 809, 104
Ashfield, W. H., & Longcope, D. W. 2021, ApJ, 912, 25
Ashfield, W. H. I., Longcope, D. W., Zhu, C., & Qiu, J. 2022, ApJ, 926, 164
Battaglia, M., & Kontar, E. P. 2012, ApJ, 760, 142
Buitrago-Casas, J. C., Martínez Oliveros, J. C., Lindsey, C., et al. 2015, SoPh, 290, 3151
Carlsson, M., Fletcher, L., Allred, J., et al. 2023, A&A, 673, A150
Carlsson, M., & Stein, R. F. 1992, ApJL, 397, L59
Christensen-Dalsgaard, J., Dappen, W., Ajukov, S. V., et al. 1996, Sci, 272, 1286
Couvidat, S., Rajaguru, S. P., Wachter, R., et al. 2012, SoPh, 278, 217
Couvidat, S., Schou, J., Hoeksema, J. T., et al. 2016, SoPh, 291, 1887
Emslie, A. G., Dennis, B. R., Shih, A. Y., et al. 2012, ApJ, 759, 71
Fisher, G. H., Canfield, R. C., & McClymont, A. N. 1985, ApJ, 289, 414
Graham, D. R., Cauzzi, G., Zangrilli, L., et al. 2020, ApJ, 895, 6
Hudson, H. S. 1972, SoPh, 24, 414
Kerr, G. S. 2022, FrASS, 9, 1060856
Kerr, G. S. 2023, FrASS, 9, 425
Kerr, G. S., Allred, J. C., Kowalski, A. F., et al. 2023, ApJ, 945, 118
Kerr, G. S., Fletcher, L., Russell, A. J. B., & Allred, J. C. 2016, ApJ, 827, 101
Kitiashvili, I. N., Couvidat, S., & Lagg, A. 2015, ApJ, 808, 59
Kosovichev, A. G. 1986, BCrAO, 75, 6
Kosovichev, A. G., Sadykov, V. M., & Stefan, J. T. 2023, ApJ, 958, 160
Kosovichev, A. G., & Zharkova, V. V. 1998, Natur, 393, 317
Kostiuk, N. D., & Pikelner, S. B. 1975, SvA, 18, 590
Kowalski, A. F. 2022, FrASS, 9, 351
Kowalski, A. F., Allred, J. C., Daw, A., Cauzzi, G., & Carlsson, M. 2017, ApJ, 836, 12
Kowalski, A. F., Hawley, S. L., Carlsson, M., et al. 2015, SoPh, 290, 3487
Lin, R. P., Dennis, B. R., Hurford, G. J., et al. 2002, SoPh, 210, 3
Livshits, M. A., Badalian, O. G., Kosovichev, A. G., & Katsova, M. M. 1981, SoPh, 73, 269
Machado, M. E., Emslie, A. G., & Avrett, E. H. 1989, SoPh, 124, 303
Macrae, C., Zharkov, S., Zharkova, V., et al. 2018, A&A, 619, A65
Monson, A. J., Mathioudakis, M., Reid, A., Milligan, R., & Kuridze, D. 2021, ApJ, 915, 16
Mravcová, L., & Švanda, M. 2017, NewA, 57, 14
Norton, A. A., Graham, J. P., Ulrich, R. K., et al. 2006, SoPh, 239, 69
Orrall, F. Q., & Zirker, J. B. 1976, ApJ, 208, 618
Pedram, E., & Matthews, S. A. 2012, SoPh, 277, 317
Pereira, T. M. D., & Uitenbroek, H. 2015, A&A, 574, A3
Procházka, O., Reid, A., Milligan, R. O., et al. 2018, ApJ, 862, 76
Reep, J. W., & Russell, A. J. B. 2016, ApJL, 818, L20
Rhodes, E. J., Jr., Reiter, J., Schou, J., et al. 2011, JPhCS, 271, 012029
Rybicki, G. B., & Hummer, D. G. 1991, A&A, 245, 171
Rybicki, G. B., & Hummer, D. G. 1992, A&A, 262, 209
Sadykov, V. M., Kosovichev, A. G., Kitiashvili, I. N., & Kerr, G. S. 2020, ApJ, 893, 24
Sadykov, V. M., Kosovichev, A. G., Sharykin, I. N., & Kerr, G. S. 2019, ApJ, 871, 2
Scherrer, P. H., Bogart, R. S., Bush, R. I., et al. 1995, SoPh, 162, 129
Scherrer, P. H., Schou, J., Bush, R. I., et al. 2012, SoPh, 275, 207
Schou, J., Scherrer, P. H., Bush, R. I., et al. 2012, SoPh, 275, 229
Sharykin, I. N., & Kosovichev, A. G. 2020, ApJ, 895, 76
Shih, A. Y., Lin, R. P., & Smith, D. M. 2009, ApJL, 698, L152
Simnett, G. M. 1986, SoPh, 106, 165
Simnett, G. M. 1995, SSRv, 73, 387
Song, Y., & Tian, H. 2018, ApJ, 867, 159
Stefan, J. T., & Kosovichev, A. G. 2020, ApJ, 895, 65
Švanda, M., Jurčák, J., Kašparová, J., & Kleint, L. 2018, ApJ, 860, 144
Švestka, Z. 1970, SoPh, 13, 471
Tamres, D. H., Canfield, R. C., & McClymont, A. N. 1986, ApJ, 309, 409
Uitenbroek, H. 2001, ApJ, 557, 389
Watanabe, K., & Imada, S. 2020, ApJ, 891, 88
Wu, H., Dai, Y., & Ding, M. D. 2023, ApJL, 943, L6
Zharkov, S., Matthews, S., Zharkova, V., et al. 2020, A&A, 639, A78